



Publication Year	2018
Acceptance in OA @INAF	2020-10-29T09:28:55Z
Title	IGR J14257-6117, a magnetic accreting white dwarf with a very strong strong X-ray orbital modulation
Authors	Bernardini, F.; DE MARTINO, Domitilla; Mukai, K.; Falanga, M.
DOI	10.1093/mnras/sty1090
Handle	http://hdl.handle.net/20.500.12386/28068
Journal	MONTHLY NOTICES OF THE ROYAL ASTRONOMICAL SOCIETY
Number	478

IGR J14257–6117, a magnetic accreting white dwarf with a very strong strong X-ray orbital modulation

F. Bernardini,^{1,2,3★} D. de Martino,^{3★} K. Mukai^{4,5} and M. Falanga⁶

¹INAF - Osservatorio Astronomico di Roma, via Frascati 33, I-00040 Monteporzio Catone, Roma, Italy

²New York University Abu Dhabi, Saadiyat Island, Abu Dhabi, 129188, United Arab Emirates

³INAF – Osservatorio Astronomico di Capodimonte, Salita Moiariello 16, I-80131 Napoli, Italy

⁴CRESST and X-Ray Astrophysics Laboratory, NASA Goddard Space Flight Center, Greenbelt, MD 20771, USA

⁵Department of Physics, University of Maryland, Baltimore County, 1000 Hilltop Circle, Baltimore, MD 21250, USA

⁶International Space Science Institute (ISSI), Hallerstrasse 6, CH-3012 Bern, Switzerland

Accepted 2018 April 24. Received 2018 April 23; in original form 2018 April 8

ABSTRACT

IGR J14257–6117 is an unclassified source in the hard X-ray catalogues. Optical follow-ups suggest it could be a Cataclysmic Variable (CV) of the magnetic type. We present the first high signal-to-noise (S/N) X-ray observation performed by *XMM-Newton* at 0.3–10 keV, complemented with 10–80 keV coverage by *Swift*/BAT, aimed at revealing the source nature. We detected for the first time a fast periodic variability at 509.5 s and a longer periodic variability at 4.05 h, ascribed to the white dwarf (WD) spin and binary orbital periods, respectively. These unambiguously identify IGR J14257–6117 as a magnetic CV of the intermediate polar (IP) type. The energy-resolved light curves at both periods reveal amplitudes decreasing with increasing energy, with the orbital modulation reaching ~ 100 per cent in the softest band. The energy spectrum shows optically thin thermal emission with an excess at the iron complex, absorbed by two dense media ($N_{\text{H}} \sim 10^{22-23} \text{ cm}^{-2}$), partially covering the X-ray source. These are likely localized in the magnetically confined accretion flow above the WD surface and at the disc rim, producing the energy-dependent spin and orbital variabilities, respectively. IGR J14257–6117 joins the group of strongest orbitally modulated IPs now counting four systems. Drawing similarities with low-mass X-ray binaries displaying orbital dips, these IPs should be seen at large orbital inclinations allowing azimuthally extended absorbing material fixed in the binary frame to intercept the line of sight. For IGR J14257–6117, we estimate $50^\circ \lesssim i \lesssim 70^\circ$. Whether also the mass accretion rate plays a role in the large orbital modulations in IPs cannot be established with the present data.

Key words: novae, cataclysmic variables – white dwarfs – X-rays: binaries – X-rays: individual: IGR J14257–6117 (aka 4PBC J1425.1-6118).

1 INTRODUCTION

Our understanding of the hard X-ray sky considerably improved because of the deep surveys carried out by the *Swift*/BAT and *INTEGRAL*/IBIS satellites at energy greater than 20 keV (Cusumano et al. 2010; Bird et al. 2016). About 20 per cent of the Galactic sources detected in these surveys are Cataclysmic Variables (CVs), among which the majority host magnetic WD primaries (MCVs). These are divided in two subclasses, depending on the WD magnetic field strength and degree of asynchronism. Polars possess stronger magnetic fields ($B \gtrsim 10^7$ G), which eventually synchronise the binary system ($P_{\text{spin}} = \omega \sim P_{\text{orb}} = \Omega$), and thus do not possess an accretion

disc. The intermediate polars (IPs) instead harbour asynchronously rotating WDs ($0.01 \lesssim P_{\omega}/P_{\Omega} < 1$; see e.g. Bernardini et al. 2017) and consequently are believed to possess weaker magnetic fields ($B \leq 10^6$ G), and thus a truncated disc at the magnetospheric radius may form. For two recent reviews on magnetic WDs and CVs, respectively, see Ferrario, de Martino & Gänsicke (2015) and Mukai (2017).

Optical follow-ups of the still unidentified sources in the BAT and IBIS catalogues provide suitable MCVs candidates (see e.g. Masetti et al. 2013; Halpern & Thorstensen 2015, and references therein). However, a proper classification resides in the X-rays and in particular in the detection of a coherent signal at the WD spin period and in the characterization of the broad-band energy spectrum (see e.g. Bernardini et al. 2012, 2014, and references therein). Short X-ray periodicities imply that the inner accretion flow follows

* E-mail: federico.bernardini@inaf.it (FB); demartino@oacn.inaf.it (DdeM)

the WD magnetic field lines, finally reaching the compact object surface, testifying that the WD is indeed magnetic. Since the flow has a supersonic velocity, a standoff shock forms and matter in the post shock region (PSR) cools (and slows) down via bremsstrahlung (hard X-ray) and cyclotron (optical/nIR) radiation (Aizu 1973; Wu, Chanmugam & Shaviv 1994; Cropper et al. 1999), the efficiency of which mainly depends on the magnetic field intensity (Woelk & Beuermann 1996; Fischer & Beuermann 2001). Cyclotron is more efficient in high intensity magnetic field systems, e.g. Polars, while IPs are bremsstrahlung-dominated systems and so, in general, harder X-ray emitters. MCV X-ray spectra are also characterized by the ubiquitous presence of a Fe K_{α} line at 6.4 keV, due to Compton reflection from the nearly neutral WD surface (Mukai 2017) and, in some cases, by a soft (~ 20 – 100 eV) X-ray blackbody emission due to thermalization of the hard X-rays, likely from the WD surface polar region. Nowadays, because of high S/N X-ray instruments such as *XMM-Newton*, the blackbody soft component is frequently detected also in IPs and not only in Polars as it originally seemed to be the case (see e.g. Bernardini et al. 2017, and reference therein).

IGR J14257–6117 is one of the still unclassified BAT and IBIS sources, for which X-ray properties were not studied yet. It was proposed to be an MCV, due to its optical spectroscopic characteristics, displaying strong emissions of Balmer, He I, and He II (Masetti et al. 2013). We here present the first simultaneous X-ray and optical data collected with *XMM-Newton* complemented with *Swift*/BAT high-energy spectral coverage that allow us to unambiguously identify it as a new member of the IP class with a particularly strong X-ray orbital modulation.

2 OBSERVATIONS AND DATA REDUCTION

2.1 *XMM-Newton* observations

IGR J14257–6117 was observed on 2017-01-20 by *XMM-Newton* with the European Photo Imaging Cameras (EPIC: PN, MOS1, and MOS2; Strüder et al. 2001; Turner et al. 2001; den Herder et al. 2001) as main instruments, complemented with simultaneous optical monitor (OM; Mason et al. 2001) photometry. The observation details are reported in Table 1. Data were processed using the Science Analysis Software version 16.1.0 and the latest calibration files available in 2017 October.

Source photon event lists and spectra for EPIC cameras were extracted from a circular region of radius 40 arcsec. The background was extracted in the same CCD where the target lies, selecting a region free from sources contamination, avoiding CCD gaps. The observation was affected by moderate particle background epochs that were conservatively removed in all instruments for the spectral analysis, while for the timing analysis, the whole data set was used.

Background-subtracted PN and MOSs light curves were produced with the task EPICLCCORR in several energy bands, with different bin size depending on the source and background rates. The event arrival times were barycentered using the task BARYCEN. Before fitting, spectra were rebinned using SPECGROUP. A minimum of 50 and 25 counts in each bin for PN and MOSs, respectively, and a maximum oversampling of the energy resolution by a factor of three were set. Phase-resolved spectra were also extracted at the minimum and maximum of the spin and orbital cycle. The response matrix and the ancillary files were generated using the tasks RMFGEN and ARFGEN, respectively. The RGS1 and RGS2 spectra were of poor S/N for a useful analysis. PN and MOSs spectra were fitted together using XSPEC version 12.9.1p package (Arnaud 1996).

The OM was operated in fast window mode using the V-band (5100–5800 Å) filter. The background-subtracted light curve was generated with the task OMFCHAIN with a bin time of 10 s and then the barycentric correction was applied.

2.2 The *Swift* observations

The *Swift*/BAT eight-channel spectra and response file from the first 66 months of BAT monitoring (Baumgartner et al. 2013) were downloaded from the publicly available archive at the Palermo BAT website.¹ IGR J14257–6117 is detected up to 80 keV, to which we restricted the spectral analysis.

3 DATA ANALYSIS AND RESULTS

3.1 Timing analysis

The results presented in this section refer to the analysis of the sum of the source event files and the background-subtracted light curves of the three EPIC cameras. Two and a half cycle of a long-term periodic variability are clearly present in the background-subtracted 0.3–12 keV light curve with superposed periodic short-term variations (Fig. 1). The X-ray light curve was heavily rebinned to wash out any short-term variation. A fit with a single sinusoid plus constant gives a period of 4.05 ± 0.06 h and a pulsed fraction (PF)² of 44 ± 2 per cent. We naturally interpreted it as the binary system orbital period ($P_{\Omega}^{X,lc}$). All uncertainty are hereafter reported at 1σ confidence level. The fit slightly improves including the first harmonic, giving a period of 4.02 ± 0.04 h. Then, the power spectra of the 0.3–12 keV source event file was computed, which showed besides the strong low-frequency peak due to the orbital modulation, two less-intense and close-by higher frequency (~ 2 mHz) peaks (Fig. 2). A phase-fitting technique (see e.g. Dall’Osso et al. 2003) was used to accurately determine the period of the stronger signal. This results in 509.5 ± 0.5 s with PF = 9.7 ± 1.6 per cent. A weaker peak at its first harmonic is also detected at 7σ confidence level, with a PF of 3.6 ± 1.6 per cent (see Table 3). We interpreted the 509.5 s period as the spin period of the accreting primary (P_{ω}^X). Since such slow rotators are only encountered in high-mass X-ray binaries and never in low mass X-ray binaries (LMXBs), and since the optical characteristics of IGR J14257–6117 are typical of CVs/LMXBs, we can safely identify it as a magnetic CV of the IP type. Its spin-to-orbit period ratio of 0.03 locates IGR J14257–6117 among the majority of asynchronous systems confirmed so far in the spin-orbital period plane (Bernardini et al. 2017). The second weaker signal is instead found at the slightly longer period of 526.8 ± 2.0 s, using the ³ task EFSEARCH (Blackburn 1995). This is interpreted as the sideband ($\omega - \Omega$, the beat) between the spin and the orbital periods. We note that this is the stronger sideband usually found in IPs. The spin-to-beat amplitude ratio is found to be 1.4 ± 0.2 (see also Section 4). From the latter, we also derive $P_{\Omega}^{X,side} = 4.30 \pm 0.53$ h, which is consistent within 1σ with the orbital period obtained from fitting the X-ray light curve. For a summary of the timing properties of IGR J14257–6117 see Table 2.

¹<http://bat.ifc.inaf.it/>

²PF = $(F_{\max} - F_{\min}) / (F_{\max} + F_{\min})$, where F_{\max} and F_{\min} are, respectively, the maximum and minimum fluxes of the sinusoid at the fundamental frequency.

³<http://heasarc.gsfc.nasa.gov/ftools/>

Table 1. Summary of main observation parameters for all instruments. Uncertainties are at 1σ confidence level.

Source Name Coordinates (J2000) ^b	Telescope	OBSID	Instrument	Date yyyy-mm-dd	UT _{start} hh:mm	T _{exp} ^a ks	Net Source Count Rate c/s
IGR J14257–6117 RA=14:25:07.58 Dec=-61:18:57.8	XMM-Newton	0780700101	EPIC-PN ^c	2017-01-20	07:02	37.5	0.475 ± 0.006
			EPIC-MOS1 ^c	2017-01-20	06:57	37.7	0.152 ± 0.002
			EPIC-MOS2 ^c	2017-01-20	06:57	37.7	0.160 ± 0.002
	Swift		OM-V ^d	2017-01-20	07:03	33.3	18.62 ± 0.13 ^e
			BAT ^f			8581	1.9 ± 0.3 × 10 ⁻⁵

^aNet exposure time.

^bCoordinates of the optical counterpart.

^cSmall window mode (thin filter applied).

^dFast window mode. The central wavelength of the V filter is 5430 Å.

^eOM instrumental magnitude.

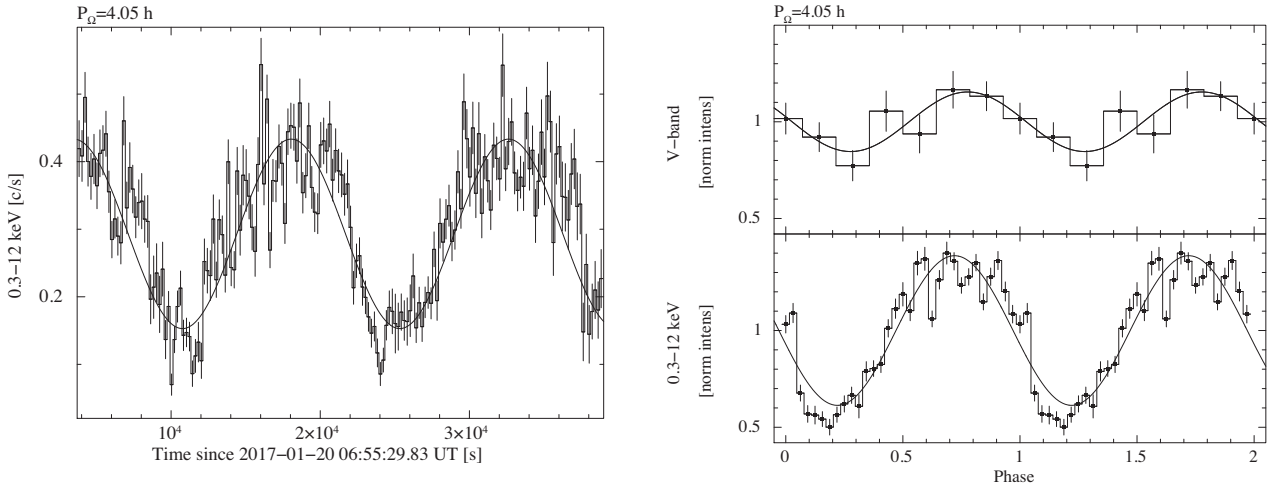
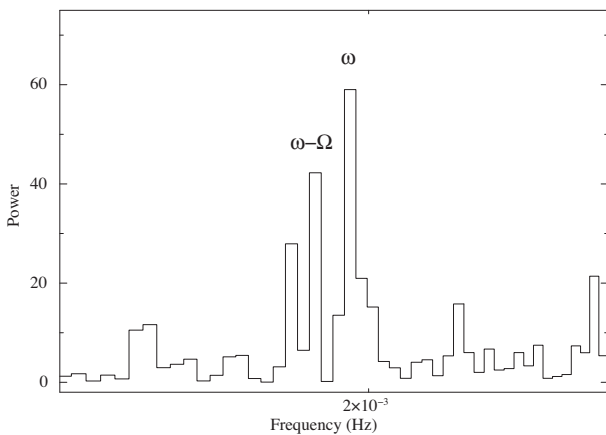
^fAll available pointings collected from 2004 December to 2010 September are summed together.

Figure 1. Left: PN plus MOSs 0.3–12 keV background-subtracted light curve of IGR J14257–6117. Short term, the WD spin, and long term, the orbital, modulations are present. Right: Background-subtracted *FP*-band (top) and 0.3–12 keV (bottom) light curves, folded at the orbital period. Two cycles are shown for plotting purposes. The reference folding time is the integer of the observation start time. In both panels, the solid line represents a sinusoid at the 4.05 h period.

Figure 2. PN 0.3–12 power spectrum zoomed in the spin, $\omega \sim 0.00196$ Hz, and beat $(\omega - \Omega) \sim 0.00190$ Hz, frequency region.

Table 2. Timing properties of IGR J14257–6117. Uncertainties are at 1σ confidence level. From left to right: P_{ω}^X (X-ray spin period); P_{side}^X (X-ray sidebands); $P_{\Omega,side}^X$ (orbital period derived from X-ray sidebands); $P_{\Omega,lc}^X$ (orbital period derived from X-ray light curve fitting); A_{ω}^X/A_{side}^X (spin to sideband X-ray amplitude ratio); P_{Ω}^A (adopted orbital period in this work).

P_{ω}^X s	P_{side}^X s	$P_{\Omega,side}^X$ h	$P_{\Omega,lc}^X$ h	A_{ω}^X/A_{side}^X	P_{Ω}^A h
509.5 ± 0.5	526.8 ± 2.0	4.30 ± 0.53	4.05 ± 0.06	1.4 ± 0.2	4.05 ± 0.06

Table 3. Pulsed fraction versus energy. Results refer to the fundamental frequency (ω , and Ω , Table 2, column 2 and 4). Uncertainties are at 1σ confidence level.

Pulsed Fraction	Pulsed Fraction				
	0.3–2 keV %	2–3 keV %	3–5 keV %	5–12 keV %	0.3– 12 keV ^a %
P_{ω}	18 ± 2	15 ± 3	7 ± 2	6 ± 2	9.7 ± 1.6
P_{Ω}	84 ± 3	60 ± 3	33 ± 2	12 ± 2	44 ± 2

^a The first harmonics have $PF_{2\omega} = 3.6 \pm 1.6$ per cent and $PF_{2\Omega} = 8 \pm 2$ per cent.

The V-band light curve instead did not show obvious periodic variability, but when folded at the X-ray orbital period a modulation is detected above 3σ confidence level. It is much weaker than that in the X-rays, its PF being only 15 per cent (Fig. 1).

To inspect spectral changes along the spin period, the background-subtracted light curves were folded at P_{ω}^X and the hardness ratios (HRs, defined as the count rate ratio in each phase bins between two selected energy ranges) were then computed. Spectral hardening at spin minimum ($\sim\varphi = 0.0-0.4$) was detected. To quantify the variation of the spin signal with respect to the energy interval, the PF was computed in five energy bands (0.3–1, 1–3, 3–5, and 5–12 keV) by fitting the modulation with a sinusoid at the fundamental frequency. The PF slightly decreases when the energy increases from a maximum 17.5 per cent (0.3–1 keV) to a minimum of 6.2 per cent (5–12 keV; Table 3 and Fig. 3). This behaviour is indicative of photoelectric absorption from neutral material localized above the X-ray emitting polar region.

Spectral variations (HRs) were also inspected as a function of the orbital period. The amplitude of the orbital modulation also decreases with increasing energy with PF of 84 per cent in the 0.3–1 keV to ~ 12 per cent in the hardest band (Table 3 and Fig. 4). The spectrum is clearly harder during orbital minima, indicating the presence of additional neutral material localized at a fixed region in the binary frame.

3.2 Spectral analysis

Fits of the broad-band average spectrum were made on the three EPIC cameras plus BAT spectra simultaneously, encompassing the range from 0.3 to 80 keV. An inter-calibration constant (fixed to one for the PN only) was used to account for instrument calibration discrepancies and spectral variability due to the fact that the BAT data are not simultaneous. All model parameters were linked between different instruments with the exception of the multiplicative constants.

XSPECIGR J14257–6117 has a thermal spectrum showing emission at the iron complex. These are characteristics generally observed in CVs and particularly in the magnetic systems, which usually have multi-temperature spectra locally absorbed by the dense cold material (see e.g. Done, Osborne & Beardmore 1995; Ezuka & Ishida 1999; Beardmore, Osborne & Hellier 2000; de Martino et al. 2004; Bernardini et al. 2012, 2013; Mukai et al. 2015; Bernardini et al. 2017). Consequently, the broad-band spectrum was fitted using a model consisting of an optically thin plasma component (MEKAL or CEMEKL in), with metal abundances (A_Z) with respect to Solar⁴ left free to vary, plus a narrow Gaussian line kept fixed at 6.4 keV accounting for the fluorescent Fe K_{α} feature, all absorbed by a total (PHABS) and two partial (PCFABS) covering columns. Indeed, a fit with only one absorbing partial covering column shows clear residuals below 1 keV. Therefore, as is the case for other IPs showing a strong orbital modulation (Bernardini et al. 2017), a second absorber was included in the spectral fit. The use of two PCFABS is also justified by the fact that the intensities of the spin and orbital modulations decrease as the energy increases and thus they are likely due to different components. We obtained statistically acceptable fits using both a multi-temperature plasma (CEMEKL) ($\chi^2_{\nu} = 0.98$, 319 d.o.f.) and a single temperature plasma (MEKAL) ($\chi^2_{\nu} = 1.03$, 319 d.o.f.) (Table 4).

⁴We set the abundance to that of the ISM from Wilms, Allen & McCray (2000)

The total absorber $N_{\text{phabs}} = 2.2 - 3.6 \times 10^{21} \text{ cm}^{-2}$ is one order of magnitude lower than that of the ISM in the direction of the source (Kalberla et al. 2005). The partial covering absorbers have densities of the order of $2-3 \times 10^{22} \text{ cm}^{-2}$ (Pcf1) and $2-3 \times 10^{23} \text{ cm}^{-2}$ (Pcf2) and their covering fractions are large: ~ 80 per cent (Pcf1) and ~ 65 per cent (Pcf2). The spectrum does not require a soft optically thick component (e.g. $kT_{\text{BB}} \sim 20 - 100 \text{ eV}$). In the case of the CEMEKL, the maximum plasma temperature is poorly constrained even not fixing to 1 the power-law α index and we derived a 3σ lower limit of 35 keV. This is much higher than that derived using MEKAL, where $kT = 18 \pm 5 \text{ keV}$. However, we note that in the latter case the temperature represents an average over the entire PSR, so the two temperatures are not expected to be consistent. We note that even if a lower limit, the CEMEKL temperature should be considered as a more reliable estimate of the shock temperature. We also checked whether a reflection component is required in the spectral fits, as indicated by the presence of the 6.4 keV iron fluorescent line ($EW = 180 \pm 20 \text{ eV}$), that would alleviate the problem of such high lower limit to the maximum temperature. Such component is however not statistically required in the spectral fits.

To obtain an estimate of the mass of the accreting WD, the broad-band continuum spectrum was also fitted (above 3 keV only) with the more physical model developed by Suleimanov, Revnivtsev & Ritter (2005), which takes into account both temperature and gravity gradients within the PSR. This gives a loosely constrained mass: $M_{\text{WD}} = 0.58 \pm 0.20 M_{\odot}$ ($\chi^2_{\nu} = 1.13$, 189 d.o.f.). It is however consistent within $\sim 1\sigma$ with the lower limit to the mass derived using the maximum CEMEKL temperature ($M_{\text{WD}} \geq 0.78 M_{\odot}$). Clearly the *Swift*/BAT spectrum is of too low quality to obtain a precise WD mass and higher S/N data are needed (see Suleimanov et al. 2016; Shaw et al. 2018).

To investigate the role of spectral parameters in generating the X-ray spin modulation, a spin-phase resolved spectroscopic analysis was performed. EPIC spectra extracted at spin maximum and minimum were fitted separately using both models presented in Table 4. N_{Hph} , A_Z , and kT (which is otherwise unconstrained) were fixed at their average spectrum best-fitting values. All other parameters, hence the two partial covering absorbers and the Gaussian normalization, were left free to vary. Likely due to the low PF (Table 3), all free parameters are constant within less than 2σ . A similar analysis was also performed on the EPIC spectra extracted at orbital maximum and minimum. This time, only the two partial covering components were left free to vary and all other model components were fixed at their average spectrum best-fitting values. The spectrum at orbital minimum is clearly harder. This is due to a significant change in both partial covering absorbers that increase at orbital minimum. In particular, in the case of both CEMEKL and MEKAL, N_{Hpc1} and N_{Hpc2} increase by a factor of ~ 3 and ~ 2 , respectively. On the other hand, the covering fraction of Pc1 significantly increases at orbital minimum, but not that of the higher density absorber (Pc2), which is found to be constant within 3σ (Table 5). Therefore, while we are unable to assess which of the two absorber is mainly responsible for the spin variability, the lower density one (Pc1) appears to be the major contributor to the orbital variability.

4 DISCUSSION AND CONCLUSIONS

IGR J14257–6117 lies very close to the Galactic plane ($b \sim -0.5^\circ$). The total Galactic absorption in the source direction is high ($1.6 \times 10^{22} \text{ cm}^{-2}$ Kalberla et al. 2005). However, N_{H} derived from spectral fits is a factor of $\sim 4-7$ lower than that pointing towards a

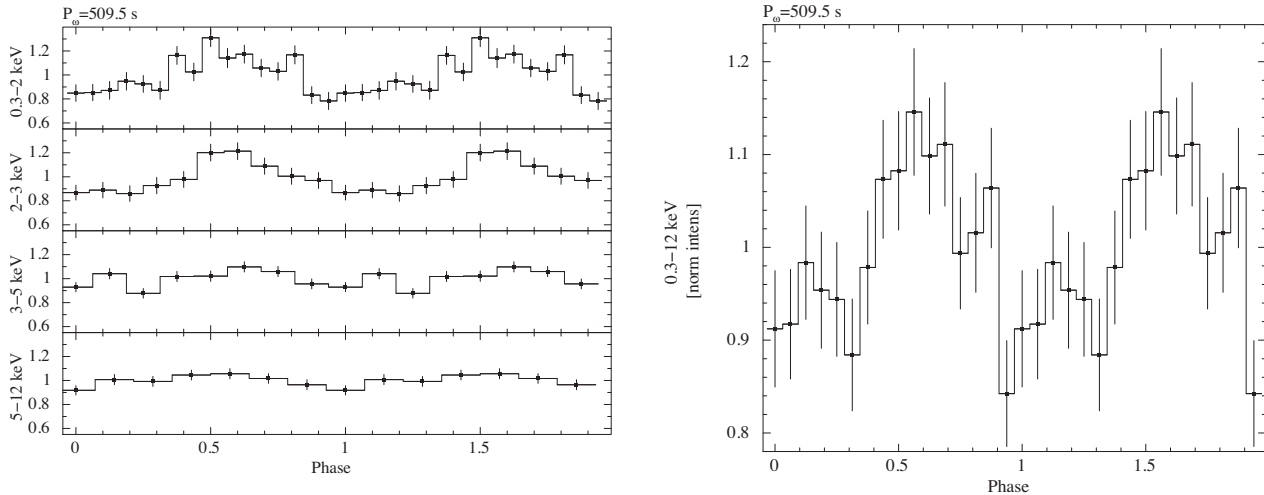


Figure 3. Left: X-ray (PN plus MOSs) normalized spin-folded light curves in different energy intervals. Energy increases from top to bottom. Two spin cycles are shown for plotting purposes. The reference folding time is the integer of the observation starting time. The PF decreases as the energy increases (cfr Table 3). Right: The spin light curve in the 0.3–12 keV band also reveals the first harmonic (see text).

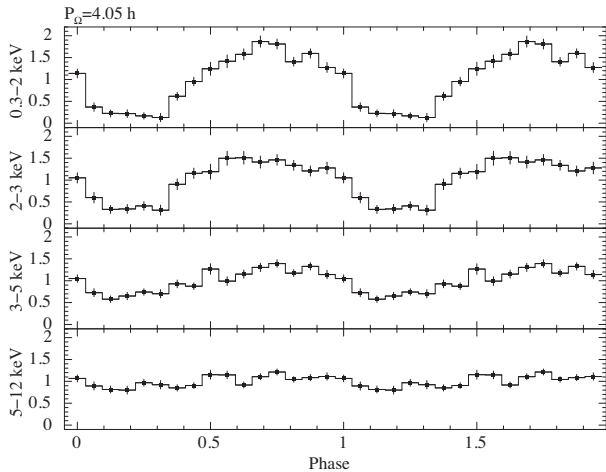


Figure 4. X-ray (PN plus MOSs) normalized orbital modulations in different energy intervals. Energy increases from top to bottom. Two cycles are shown for plotting purposes. The reference folding time is the integer of the observation starting time (Table 1). The X-ray PF decreases as the energy increases (Table 3).

close-by Galactic object (see also Masetti et al. 2013, for a similar conclusion derived from *V*-band absorption). To get an estimate of the source distance we use near-IR data. IGR J14257–6117 is listed in the 2MASS (Two Micron All Sky Survey) catalog as 2MASS J14250758–6118578. It is only detected in the *J*-band, with $J = 16.194 \pm 0.096$ mag (upper limits of $H > 14.8$ and $K > 14.4$ mag). We dereddened it assuming $N_H = 2.9 \times 10^{21} \text{ cm}^{-2}$ (as derived from the average X-ray spectrum), which translates (Güver & Özel 2009) in $A_V = 1.3$ (and $A_J = 0.34$). For a CV in a 4.05 h orbit, a M3.5 donor with $M_J = 7.1$ mag is expected (Knigge, Baraffe & Patterson 2011). Assuming that the donor is totally contributing to the *J*-band flux (when dereddened, $J = 15.85$ mag) we derive a distance $d = 563 \pm 225$ pc (assuming a 40 per cent uncertainty). Adopting this distance, we estimate the accretion luminosity as: $L_{\text{acc}} = GMM/R \sim L_{X,\text{bol}} \sim 7.6 \times 10^{32} \text{ erg/s}$, where $L_{X,\text{bol}}$ is evaluated over a wide range 0.01–100 keV. Adopting a conservative lower limit to the WD mass of $0.58 M_\odot$, this translates into an

upper limit to the mass accretion rate, $\dot{M} \lesssim 1.4 \times 10^{-10} M_\odot \text{ yr}^{-1}$. If the distance is much larger, as from the upper envelope of the distance estimate (~ 900 pc), the mass accretion rate is bounded to an upper limit of $\lesssim 4 \times 10^{-10} M_\odot \text{ yr}^{-1}$. As in the case of the majority of IPs (e.g. see Bernardini et al. 2012, 2017), \dot{M} is found to be lower than the secular mass transfer rate predicted by models of the present-day CV population, in the case of a binary above the orbital period gap evolving through magnetic braking in a 4-h orbit ($\dot{M} \sim 5 \times 10^{-9} M_\odot \text{ yr}^{-1}$; Howell, Nelson & Rappaport 2001). These estimates should be considered with caution because a non-negligible fraction of the X-ray emission could be reprocessed in the accretion flow (e.g. the magnetically confined accretion flow above the shock and the accretion disc) and radiated at lower energies. Low mass transfer rates have also been found in an increasing number of CVs above the 2–3 h orbital period gap using the effective temperature of the unheated primary, when detected (see Pala et al. 2017).

IGR J14257–6117 is then an IP above the gap with a spin-to-orbit period ratio $P_\omega/P_\Omega \sim 0.03$, and its position in the P_ω versus P_Ω plane (see Fig. 6, left-hand panel in Bernardini et al. 2017) falls where the majority of the systems of its class lie, confirming that the observed present-day population of IPs is dominated by systems above the period gap. Whether the paucity of IP systems below the gap (see also Pretorius & Mukai 2014) is due to selection effects in their discovery (faint X-ray sources) or indeed almost all IPs evolve into low-field Polars still remains an open problem to be addressed with future sensitive X-ray survey missions such as *eROSITA*.

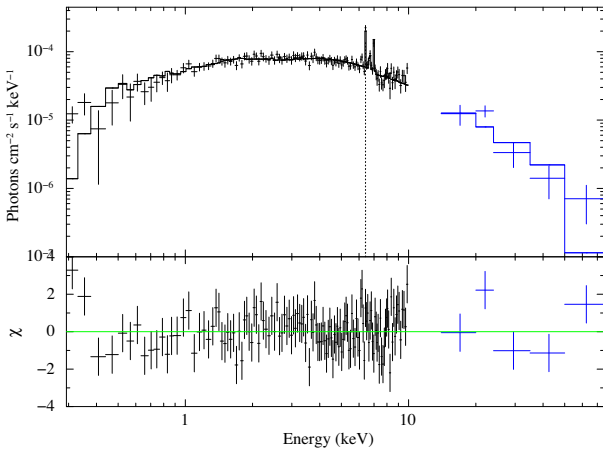
IGR J14257–6117 has been found to show the spin, the beat, and orbital modulations. The spin variability is found to be much weaker than that at the orbital period. The energy dependence of the rotational modulation is a characteristic also found in the majority of IP systems and consistent with the accretion curtain scenario (Rosen, Mason & Cordova 1988) where the magnetically confined accretion occurs in a curtain-shaped flow. The hardening at spin minimum is due to the curtain pointing towards the observer when the absorption in the pre-shock flow is maximum. The spin variability indicates that matter is accreted via a disc. However, the detection of a non-negligible variability at the $\omega - \Omega$ sideband implies that material is also overflowing the disc at a fraction of ~ 45 per cent of the total flow. Such hybrid accretion geometry is also observed in many other

Table 4. Parameters of the best fit models to the averaged broad-band spectrum. The absorbed 0.3–10 keV and unabsorbed bolometric (0.01–200 keV) fluxes are reported in the last two columns. Uncertainties are at 1σ confidence level.

mod.	$N_{\text{H}_{\text{pb}}}$ 10^{22} cm^{-2}	$N_{\text{H}_{\text{pc1}}}$ 10^{22} cm^{-2}	cvf %	$N_{\text{H}_{\text{pc2}}}$ 10^{22} cm^{-2}	cvf %	kT keV	n 10^{-3}	A_{Z}	EW keV	$F_{0.3-10}$ 10^{-12} $\text{erg}/\text{cm}^2/\text{s}$	$F_{\text{X, bol}}$ 10^{-12} $\text{erg}/\text{cm}^2/\text{s}$	χ^2/dof
cemek ^a	0.22 ± 0.10	$1.87^{+0.32}_{-0.23}$	81 ± 3	20 ± 2	65 ± 4	>35 ^b	10.0 ± 0.5	1.3 ± 0.3	0.18 ± 0.02	4.6 ± 0.1	~ 19.7	$0.98/319$
mek	0.36 ± 0.07	3.1 ± 0.8	74 ± 3	28 ± 6	63 ± 3	18 ± 2	5.3 ± 0.4	0.68 ± 0.13	0.18 ± 0.01	4.6 ± 0.1	~ 21.1	$1.03/319$

^a Multi-temperature power-law index α fixed to 1.^b 3σ lower limit. The best fitting value is 80 keV, but poorly constrained.**Table 5.** Spectral parameters at maximum (Max) and minimum (Min) of the orbital modulation (Orb.). All other parameters are fixed to their average spectrum best-fitting values. Uncertainties are at 1σ confidence level.

model	Orb.	$N_{\text{H}_{\text{pc1}}}$ 10^{22} cm^{-2}	cvf %	$N_{\text{H}_{\text{pc2}}}$ 10^{22} cm^{-2}	cvf %	$F_{0.3-10}$ 10^{-12} $\text{erg cm}^{-2} \text{ s}^{-1}$	χ^2/dof
cemek	Max	1.5 ± 0.2	80 ± 1	15.2 ± 1.2	58 ± 2	5.0 ± 0.1	$1.07/275$
	Min	4.6 ± 0.8	92 ± 1	35 ± 4	71 ± 5	3.4 ± 0.1	$1.04/127$
mek	Max	2.4 ± 0.3	70 ± 2	25 ± 2	60 ± 2	5.1 ± 0.1	$1.10/275$
	Min	6.4 ± 1.0	91 ± 1	48 ± 5	71 ± 4	3.4 ± 0.1	$1.08/127$

**Figure 5.** Broadband unfolded spectrum of IGR J14257–6117. Post fit residuals are shown in the lower panel. The black points are *XMM-Newton*/PN data (0.3–10 keV), the blue points are *Swift*/BAT data (15–80 keV). The fit is made simultaneously on all EPIC cameras, but for the sake of readability, only the PN data are shown. The dotted line mark the 6.4 keV Gaussian component, while the solid line is the composite model.

IPs, indicating it is not so uncommon in these systems (Bernardini et al. 2012; Hellier 2014; Bernardini et al. 2017).

IGR J14257–6117 is also one of the members of the IP class that shows an X-ray light curve strongly modulated at the orbital period. Energy-dependent X-ray orbital modulations appear to be a common property of IPs and, in some systems, also found to vary on time-scales of years (see e.g. Parker, Norton & Mukai 2005; Bernardini et al. 2017), with the unique case of FO Aqr that entered in a low state in spring 2016 and recovered its high state at the end of 2016 (Kennedy et al. 2016, 2017). Long-term changes of the amplitudes of spin, orbital, and beat variabilities were also observed in IPs at both X-rays (Norton et al. 1997; Beardmore et al. 1998; Staude et al. 2008) and UV/optical wavelengths (de Martino et al. 1999), accompanied by moderate changes in their brightness. Such changes are ascribed to variations in the mass accretion rate, which in turn modifies the accretion geometry. In particular changes in the spin-to-beat amplitudes are interpreted as an increase or decrease of

the disc-overflow contribution (see Hellier 2014). The presence of a strong orbital and energy-dependent modulation indicates absorbing material fixed in the orbital frame. The lack of a spectroscopic orbital ephemeris does not allow us to correctly locate the superior conjunction of the donor or the WD but, drawing similarities with other IPs also showing energy-dependent orbital modulations, this material should be located at the outer disc rim, where the stream of material from the companion impacts the disc. The presence of a disc overflow further supports the scenario of an azimuthally extended region.

Disc structures are also found in LMXBs seen at relatively high inclinations, the so-called ‘dippers’, which show periodic dips at the orbital period, generally attributed to partial obscuration of the X-ray emitting source by a thickened ionized region of the accretion disc (Diaz Trigo et al. 2006). Sometimes the occurrence of dips is intermittent, as observed in Aql X-1 in two occasions (Galloway et al. 2016). In the ultra-compact binary 4U 1820–303 an orbital modulation is observed with amplitude changing with X-ray luminosity, but is not energy dependent (Zdziarski et al. 2007). Such variations have been claimed to arise from changes in the mass accretion rate due to disc precession in both systems. Similar interpretation of a precessing disc was given for the IPs showing X-ray orbital modulations with amplitude changing with time (Parker et al. 2005; Norton & Mukai 2007). Whether the changes in mass accretion rate are due to disc precession or to variable mass transfer rate from the donor star is however unclear. The X-ray emission in these systems would then be viewed through higher density columns at different epochs, along the precessing period. The high density material (up to 10^{23} cm^{-2}) would then produce a large orbital modulation, expected to reach 100 per cent at 1 keV, and a significant modulation up to 10 keV (Norton & Watson 1989; Parker et al. 2005). In IGR J14257–6117 we have inferred the presence of two local partial covering absorbers with high column densities: $N_{\text{H,pc1}} \sim 2 \times 10^{22} \text{ cm}^{-2}$, $\text{cvf1} \sim 80$ per cent and $N_{\text{H,pc2}} \sim 2 \times 10^{23} \text{ cm}^{-2}$, $\text{cvf2} \sim 60$ per cent. With the present data we are unable to definitively assess which of them is responsible for the weaker spin amplitude variability and the large orbital modulation, although the lower density complex absorber (pcf1) appears to be the major contributor to the orbital modulation.

We then inspected whether the large amplitude orbital variability in IGR J14257–6117 fits into a general scheme of IPs with a modulation that increases with the increasing X-ray luminosity and thus mass accretion rate. An essential parameter to assess this is the binary inclination, which is not well determined in IPs, but it is proposed to be in excess of 60° in all IPs showing X-ray orbital modulations (Parker et al. 2005). We then collected the modulation depths,⁵ as measured from ASCA data in the 0.7–2 keV range, for

⁵ It is defined as the peak-to-peak amplitude of the sinusoid used to fit each light curve folded at the orbital period, divided by the maximum flux of the sinusoid. The mean level, amplitude, and phase of the sinusoid were left free to vary in the fit.

12 IPs. For these systems we also collected the distance estimates and when available their binary inclination⁶ (see Section A). We enlarged the sample to 17 sources by including five additional systems found by us to show orbital modulations: IGR J14257–6117, *Swift* J0927.7–6945 (henceforth J0927), and *Swift* J2113.5+5422 (henceforth J2113) (Bernardini et al. 2017), as well as V709 Cas and NY Lup studied in Mukai et al. (2015). For consistency, we evaluated the modulation depth as defined in Parker et al. (2005). For all sources in the sample, we computed their unabsorbed bolometric luminosity in the 0.01–100 keV range (see Section A) as a proxy of the mass accretion rate at the epoch of the observation. For V1223 Sgr, V405 Aur, and PQ Gem there are two epochs of observations and thus both are included in the analysis. As shown in Table A1, IGR J14257–6117 and FO Aqr (in 1997) have shown the strongest orbital modulation depth (almost 100 per cent), although J0927, BG CMi have consistent modulation depths within their uncertainties. These are found at relatively high luminosities ($1 - 6 \times 10^{33}$ erg s⁻¹), but only FO Aqr and BG CMi are known to be moderately high inclination systems. Possibly BG CMi, similar to FO Aqr, has a higher binary inclination than the lower limit estimated so far. Similar or even higher luminosity levels are however found in other systems showing weaker (20–60 per cent) orbital modulation depths. While distances could strongly affect the derived luminosities, the fact that systems at low inclinations, such as NY Lup, YY Dra, and V1223 Sgr, have weak orbital modulation depths may suggest that the binary inclination plays a key role in shaping the orbital modulation in these systems. For the three IPs for which two epochs are available, no clear relation with luminosity is found, but small changes in depths could indicate slight variations in the azimuthal structure of the responsible region. Considering only systems for which the detection of an orbital modulation is above 3σ , we are left with nine IPs for which no clear relation with the luminosity, and thus the mass accretion rate, is found.⁷ Unless true distances are greatly different, the lack of a statistically significant correlation of the orbital modulation depths with the luminosity could favour a scenario where the sample, although still poor, would be mainly constituted by moderate-high binary inclination ($\gtrsim 50 - 60^\circ$) systems, with the only exception being the peculiar low-inclination TX Col (see Ferrario & Wickramasinghe 1999). The lack of X-ray eclipses in IGR J14257–6117, J2113, and J0927 also poses an upper limit to the inclination of these systems, $i \lesssim 70^\circ$. Future precise parallaxes of the sample that will soon be available with *Gaia* DR2 release will allow firmer conclusions.

We here finally note that the discovery of IGR J14257–6117 as an additional strongly orbital-modulated IP makes these systems ideal targets to be monitored for possible variations in their orbital modulation depth. This would allow to assess whether this feature is stable or may hint to a precessing disc or changes in the mass accretion rate. Further observations, especially optical spectroscopy, will be extremely useful to determine the true inclination of this binary.

ACKNOWLEDGEMENTS

FB is funded by the European Union’s Horizon 2020 research and innovation programme under the Marie Skłodowska-Curie grant

⁶Koji Mukai Website (<https://asd.gsfc.nasa.gov/Koji.Mukai/iphome/iphome.html>)

⁷We do not attempt to relate directly the orbital depth with the mass accretion rate due to the additional uncertainty in the WD mass estimates

agreement n. 664931. DdM acknowledges financial support from the Italian Space Agency and National Institute for Astrophysics, ASI/INAF, under agreements ASI-INAF I/037/12/0 and ASI-INAF n.2017-14-H.0. This work is based on observations obtained with *XMM-Newton*, an ESA science mission with instruments and contributions directly funded by ESA Member States; with *Swift*, a National Aeronautics and Space Administration (NASA) science mission with Italian participation. This work has also made use of the the 2MASS, a joint project of the University of Massachusetts and the Infrared Processing and Analysis Center (IPAC)/Caltech, funded by NASA and the NSF.

REFERENCES

- Aizu K., 1973, *Prog. Theor. Phys.*, 49, 1184
 Ak T., Bilir S., Ak S., Eker Z., 2008, *MNRAS*, 13, 133
 Arnaud K. A., 1996, in Jacoby G. H., Barnes J., eds, *ASP Conf. Ser.*, 101, San Francisco, p. 17
 Baumgartner W., Tueller J., Markwardt C., Skinner G., Barthelmy S., Mushotzky R., Evans P., Gehrels N., 2013, *ApJS*, 297, 19
 Beardmore A. P., Mukai K., Norton A. J., Osborne J. P., Hellier C., 1998, *MNRAS*, 297, 337
 Beardmore A. P., Osborne J. P., Hellier C., 2000, *MNRAS*, 315, 307
 Bernardini F., de Martino D., Falanga M., Mukai K., Matt G., Bonnet-Bidaud J.-M., Masetti N., Mouchet M., 2012, *A&A*, 542, A22
 Bernardini F. et al., 2013, *MNRAS*, 435, 2822
 Bernardini F., de Martino D., Mukai K., Falanga M., 2014, *MNRAS*, 445, 1403
 Bernardini F., de Martino D., Mukai K., Russell D. M., Falanga M., Masetti N., Ferrigno C., Israel G., 2017, *MNRAS*, 470, 4815
 Bird A. J. et al., 2016, *ApJS*, 223, 15
 Blackburn J. K., 1995, in Shaw R. A., Payne H. E., Hayes J. J. E. eds, *ASP Conf. Ser.*, 77, San Francisco, p. 367
 Bonnet-Bidaud J.-M., Haberl F., Ferrando P., Bennie P., Kendziorra E., 2001, *A&A*, 365, 282
 Cropper M., Wu K., Ramsay G., Kocabiyyik A., 1999, *MNRAS*, 306, 684
 Cusumano G., La Parola V., Segreto A., Ferrigno C., Maselli A., Sbarufatti B., Romano P. e., 2010, *A&A*, 524, 64
 Dall’Osso S., Israel G., Stella L., Possenti A., Peruzzi E., 2003, *ApJ*, 599, 485
 de Martino D., Silvotti R., Buckley D. A. H., Gänsicke B. T., Mouchet M., Mukai K., Rosen S. R., 1999, *A&A*, 350, 517
 de Martino D., Matt G., Belloni T., Haberl F., Mukai K., 2004, *A&A*, 415, 1009
 den Herder J. W. et al., 2001, *A&A*, 365, L7
 Diaz Trigo M., Parmar A., Boirin L., Mendez M., Kaastra J. S., 2006, *A&A*, 445, 179
 Done C., Osborne J., Beardmore A., 1995, *MNRAS*, 276, 483
 Ezuka H., Ishida M., 1999, *ApJS*, 120, 277
 Ferrario L., Wickramasinghe D. T., 1999, *MNRAS*, 309, 517
 Ferrario L., de Martino D., Gänsicke B. T., 2015, *Space Sci. Rev.*, 191, 111
 Fischer A., Beuermann K., 2001, *A&A*, 373, 211
 Galloway D. K., Ajamyan A. N., Upjohn J., Stuart M., 2016, *MNRAS*, 461, 3847
 Güver T., Özel F., 2009, *MNRAS*, 400, 2050
 Halpern J. P., Thorstensen J. R., 2015, *AJ*, 150, 170
 Hellier C., 2014, *EPJ Web Conf.*, 64, 07001
 Howell S. B., Nelson L. A., Rappaport S., 2001, *ApJ*, 550, 897
 Kalberla P. M. W., Burton W. B., Hartmann D., Arnal E. M., Bajaja E., Morras R., Pöppel W. G. L., 2005, *A&A*, 440, 775
 Kennedy M. R., Garnavich P., Breedt E., Marsh T. R., Gänsicke B. T., Steeghs D., Szkody P., Dai Z., 2016, *MNRAS*, 459, 3622
 Kennedy M. R., Callanan P., Garnavich P. M., Fausnaugh M., Zinn J. C., 2017, *MNRAS*, 466, 2202
 Knigge C., Baraffe I., Patterson J., 2011, *ApJS*, 194, 28
 Masetti N. et al., 2013, *A&A*, 556, A120

- Mason K. O. et al., 2001, *A&A*, 365, L36
 Mukai K., 2017, *PASP*, 129, 062001
 Mukai K., Rana V., Bernardini F., de Martino D., 2015, *ApJ*, 807, L30
 Norton A. J., Mukai K., 2007, *A&A*, 472, 225
 Norton A. J., Watson M. G., 1989, *MNRAS*, 237, 853
 Norton A. J., Hellier C., Beardmore A. P., Wheatley P. J., Osborne J. P., Taylor P., 1997, *MNRAS*, 289, 362
 Pala A. F. et al., 2017, *MNRAS*, 466, 2855
 Parker T. L., Norton A. J., Mukai K., 2005, *A&A*, 439, 213
 Pretorius M. L., Mukai K., 2014, *MNRAS*, 442, 2580
 Rosen S. R., Mason K. O., Cordova F. A., 1988, *MNRAS*, 231, 549
 Shaw A. W., Heinke C. O., Mukai K., Sivakoff G. R., Tomsick J. A., Rana V., 2018, *MNRAS*, 476, 554
 Staude A., Schwobe A. D., Schwarz R., Vogel J., Krumpel M., Nebot Gomez-Moran A., 2008, *A&A*, 486, 899
 Strüder L. et al., 2001, *A&A*, 365, L18
 Suleimanov V., Revnivtsev M., Ritter H., 2005, *A&A*, 435, 191
 Suleimanov V., Doroshenko V., Ducci L., Zhukov G. V., Werner K., 2016, *A&A*, 591, A35
 Turner M. J. L. et al., 2001, *A&A*, 365, L27
 Wilms J., Allen A., McCray R., 2000, *ApJ*, 542, 914
 Woelk U., Beuermann K., 1996, *A&A*, 306, 232
 Wu K., Chanmugam G., Shaviv G., 1994, *ApJ*, 426, 664
 Zdziarski A. A., Gierliński M., Wen L., Kostrzewa Z., 2007, *MNRAS*, 377, 1017

APPENDIX A: ORBITAL MODULATION DEPTHS AND BOLOMETRIC LUMINOSITIES OF THE IP SAMPLE

To explore a possible relation among the orbital modulation depth, the bolometric luminosity, and the inclination, we collected the sources presented in Parker et al. (2005) that were observed with *ASCA*. We selected *ASCA* data since, due to the effect of the photoelectric absorption, our analysis concentrates in the soft X-ray bands, where the orbital modulations are higher. Two of these sources were also later observed jointly by *XMM-Newton* and *NuSTAR*, namely V1223 Sgr and NY Lup, together with V709 Cas (Mukai et al. 2015). We also included those data in our analysis. Finally, we add three other IPs that were recently observed by *XMM-Newton* to show X-ray orbital modulations, namely J0927 and J2113 (Bernardini et al. 2017), plus IGR J14257–6117 (Table A1). For the above five sources, the orbital modulation depths, as defined by Parker et al. (2005), were computed in the same 0.2–7 keV range, for uniformity.

APEC In order to estimate the source bolometric (0.01–100 keV) fluxes we proceeded as follow. For those sources observed with *ASCA*, we downloaded the public archival BAT 105-month spectra.⁸ Since the spectra span a long period of time that does not overlap

Table A1. Main parameters of the IP sample: the orbital modulation depth in the 0.2–7 keV range, the bolometric (0.01–100 keV) luminosity (L), the distance (d), and binary inclination, when available. The instrument(s) (ins.) used to perform the observation is also reported, where A stands for *ASCA*, X+N for *XMM-Newton*+*NuSTAR*, and X for *XMM-Newton*.

Source	ins.	depth %	L 10^{32} erg s $^{-1}$	d pc	i^b deg
V1025 Cen	A	3 ± 3	2.12 $^{+2.2}_{-1.4}$	230 $^{+70}_{-100}$ [1]	–
BG CMi	A	82 ± 9	42.0 $^{+13.3}_{-16.3}$	553 $^{+286}_{-34}$ [1]	55–75
V1223 Sgr	A	28 ± 3	127.5 $^{+56.6}_{-37.3}$	527 $^{+54}_{-43}$ [2]	16–40
	X+N	11 ± 2	178.3 $^{+97.8}_{-70.4}$		
V2400 Oph	A	4 ± 2	26.8 $^{+42.0}_{-16.3}$	280 $^{+150}_{-100}$ [2]	10:
AO Psc	A	47 ± 5	20.1 $^{+39.9}_{-13.0}$	330 $^{+120}_{-280}$ [2]	60:
YY Dra	A	9 ± 4	1.1 $^{+0.7}_{-0.6}$	155 $^{+35}_{-25}$ [3]	42±5
V405 Aur	A	6 ± 2	26.0 $^{+59.8}_{-17.5}$	380 $^{+210}_{-130}$ [2]	–
	A	21 ± 4	17.4 $^{+15.3}_{-11.3}$		
FO Aqr	A	102 ± 13	61.5 $^{+106.0}_{-39.7}$	450 $^{+240}_{-160}$ [2]	65:
PQ Gem	A	10 ± 3	55.0 $^{+125.7}_{-38.5}$	510 $^{+160}_{-180}$ [2]	–
	A	3 ± 4	34.6 $^{+67.6}_{-27.5}$		
TV Col	A	47 ± 6	42.0 $^{+7.3}_{-7.3}$	368 $^{+17}_{-15}$ [2]	70:
TX Col	A	58 ± 6	43.0 $^{+59.7}_{-39.7}$	591 $^{+185}_{-175}$ [1]	<25
V1062 Tau	A	35 ± 12	325.9 $^{+423.2}_{-198.0}$	1400 $^{+700}_{-500}$ [2]	–
V709 Cas	X+N	19 ± 1	7.0 $^{+1.6}_{-1.4}$	230 $^{+20}_{-15}$ [4]	–
NY Lup	X+N	<10	100.8 $^{+108.5}_{-54.8}$	690 $^{+150}_{-150}$ [3]	25–58
J0927	X	91 ± 2	14.5 $^{+10.1}_{-10.1}$	670 $^{+268}_{-268}$ [5] ^a	–
J14257	X	95 ± 3	8.3 $^{+6.2}_{-6.2}$	563 $^{+225}_{-225}$ [6] ^a	–
J2113	X	76 ± 1	19.5 $^{+59.3}_{-14.4}$	750 $^{+300}_{-300}$ [5] ^a	–

^a We assumed a 40 per cent uncertainty on the distance.

^b See Koji Mukai Website and more reference therein (<https://asd.gsfc.nasa.gov/Koji.Mukai/iphone/iphone.html>).

Distances from: [1] Ak et al. (2008) [2]; Parker et al. (2005); [3] Koji Mukai Website; [4] Bonnet-Bidaud et al. (2001); [5] Bernardini et al. (2017); [6] This work. Uncertain distances are reported with a side colon.

with the *ASCA* observations, they have been fitted alone. The fits were performed once with a one temperature collisionally ionized diffuse gas and once with a cooling flow model (*APEC* and *MKCFLOW* in *XSPEC*, respectively). We here note that a similar result within uncertainties could be obtained using a *CEMEKL* model. Then, we fitted the *ASCA* spectra with the *APEC* model and *MKCFLOW*, with a complex absorber as necessary to achieve a reasonable fit. Then we re-fitted the *ASCA* spectra fixing the temperature to the best-fitting values first found for the BAT spectra alone. To be conservative, we used the range of luminosity obtained from the minimum and maximum fluxes among the four spectral fits to the *ASCA* spectra. For the three sources simultaneously observed with *XMM-Newton* and *NuSTAR*, the broad-band spectrum was fitted with similar models. For J0927, J2113, and IGR J14257–6117 we used instead their best-fitting broad-band spectral models presented in Bernardini et al. (2017) and in this work, respectively. We here note that for those IPs showing a soft X-ray blackbody component (see Bernardini et al. 2017), the range of minimum and maximum bolometric fluxes encompass this component.

Then luminosities were computed using distances reported in the literature. When available, the estimate of the binary inclination were also collected (see Table A1).

This paper has been typeset from a $\text{\TeX}/\text{\LaTeX}$ file prepared by the author.

⁸<https://swift.gsfc.nasa.gov/results/bs105mon/>